Image formation and tomogram reconstruction in optical coherence microscopy

Martin Villiger* and Theo Lasser

Laboratoire d'Optique Biomédicale, Ecole Polytechnique Fédérale de Lausanne, Station 17, CH-1015 Lausanne, Switzerland
**Corresponding author: martin.villiger@epfl.ch*

Received July 12, 2010; accepted July 29, 2010;
posted August 18, 2010 (Doc. ID 131399); published September 22, 2010

In this work we present a model for image formation in optical coherence microscopy. In the spectral domain detection, each wavenumber has a specific coherent transfer function that samples a different part of the object's spatial frequency spectrum. The reconstruction of the tomogram is usually accurate only in a short depth of field. Using numerical simulations based on the developed model, we identified two distinct mechanisms that influence the signal of out-of-focus sample information. Besides the lateral blurring induced through defocusing, an additional axial envelope contributing equally to the signal degradation was found. © 2010 Optical Society of America

OCIS codes: 180.1655, 170.4500, 110.6955, 110.6880, 110.1650.

1. INTRODUCTION

Optical coherence tomography (OCT) is a biomedical imaging technique that provides cross-sectional views of the subsurface microstructure using spectral interferometry. It has received considerable interest as a minimally invasive imaging technique. Detection in the spectral or Fourier domain (FDOCT), recording interferograms of a large number of wavenumber-channels in parallel or consecutively, as in swept source OCT, allows reconstructing the sample's depth structure at a given lateral scanning position in a parallel fashion without axial scanning. Compared to point scanning techniques, this results in an important speed advantage, and paired with the fundamental signal benefit provided by the detection in the Fourier domain [1], it makes FDOCT a confirmed tool for minimally invasive *in vivo* applications.

Whereas the axial resolution of OCT is determined by the coherence length of the employed light source, the lateral resolution is specified by the numerical aperture (NA) of the imaging optics. Classical OCT uses focusing optics resulting in a limited lateral resolution of 10–20 μm, yet providing a near constant lateral definition over a long axial range. The combination of OCT with high NA optics results in a combined depth sectioning by means of the coherence and the confocal gates and is termed optical coherence microscopy (OCM) [2]. This combined depth sectioning is advantageous in strongly scattering media. It resolves fine sample structures [3], and the available phase information can be used for phase imaging of thin cell samples [4,5]. However, the short depth of field (DOF) imposed by the confocal gate compromises Fourier domain optical coherence microscopy's (FDOCM)'s parallel depth extraction, and it necessitates three-dimensional scanning to acquire the volumetric sample structure.

Many attempts have been made to overcome this fundamental dilemma and to take advantage of high lateral resolution and parallel depth extraction at the same time. Strategies to circumvent this compromise involve, on one hand, digital correction of the induced artifacts [6–8] and, on the other hand, hardware solutions [9–12]. Following the same reasoning, we previously described an extended focus scheme for FDOCM [13].

The works on digital correction often use Gaussian optics approximations to deduce the proposed algorithms. Ralston *et al.* [8,14] developed a more advanced signal model for the formulation of the inverse problem that reconstructs a corrected tomogram. While the first models were still based on Gaussian paraxial optics, they later extended the formulation to non-paraxial optics [15]. In general, most of the proposed hardware solutions aimed at the production of an elongated focus defining a needle-like probing volume. Typically, these attempts ignore, however, the underlying image formation and tomogram reconstruction.

Compared to confocal microscopy, for which the image formation was studied in great detail and is well documented in the literature, there exists relatively little work on image formation in OCT. Moreover, the tomograms obtained in FDOCT depend on both the image formation, i.e., the signal recorded, and the tomogram reconstruction. Many authors used a simple layered media approach and defined the sample as a stack of regions of homogenous refractive indices with discrete interfaces defining a reflectivity depth-profile [16]. Fercher *et al.* [17] applied the first order Born diffraction for their signal model and defined the scattering potential as the sample structure. It should be considered, however, that this sample structure comprises the squared wavenumber, which inevitably has implications when reconstructing the FDOCT signal and taking the Fourier transformation along the wavenumber coordinate. Sheppard *et al.* [18] showed an interesting analysis of the image formation in low-coherence and confocal interference microscopes,

starting with the image formation in a conventional microscope. Yet, that report neither treated the physical origin of the structural signal nor discussed the specific effects of FDOCT, because it considered a time-domain system. A notable work by Coupland and Lobera [19] compared the image formation in holography, three-dimensional microscopy, and OCT, describing them as a linear filtering process. Although OCT in the low NA approximation can indeed be described as a linear filtering, this is not sufficient in general.

Here, we present a model for image formation in OCT, and especially OCM in the Fourier domain, using the principle of the generalized aperture, introduced by McCutchen [20], and the coherent transfer function (CTF), known from the pioneer work by Sheppard *et al.* [21] and Gu [22]. The FDOCT system can be interpreted as a multiplexed interference microscope, where each wavenumber-channel of the detector has its distinct CTF. If a confocal three-dimensional scan was performed, the signal recorded in each wavenumber-channel would be indeed the result of the linear filtering of the sample with the channel's specific CTF. But FDOCM attempts to reconstruct the three-dimensional sample structure from the wavenumber multiplexed signal, without scanning in the axial direction. The sampling of the spatial frequency spectrum is in this case defined by the exact shape of the channel's specific CTFs and becomes, in general, increasingly flawed for larger NAs.

Based on this model, tomograms were simulated to evidence the precise effect of the system CTFs. We show that the DOF has two origins. First, the CTF has in general a curved shape, which introduces a defocusing and results in the lateral blurring of the out-of-focus structures. Second, the CTF has a finite support, i.e., a span with tolerable transmission values, along the axial spatial frequencies and confuses the signal within this window. In the reconstructed tomogram, this is manifested in an additional axial amplitude envelope. In the case of identical Gaussian optics in both the illumination and the detection paths, these two mechanisms contribute equally to the signal degradation.

Based on these simulation results, we discuss the ideal CTF for FDOCT, producing an extended DOF. The formulation that we present here is developed in a general form and considers also decoupled and independently defined illumination and detection paths. This allows testing specific optical implementations that strive toward this ideal CTF.

2. THEORY

A. Description of the Setup

As displayed in Fig. 1, a spectrometer-based spectral domain OCT system is considered. Light from a broadband illumination source is delivered through a single mode fiber, collimated, and split by a free-space beam splitter into reference and sample arms. In the sample arm the light is focused into the sample by means of a sample objective. Classical OCT uses lenses with relatively long focal lengths resulting in low NAs. In contrast, OCM employs objectives with significantly larger NAs. A scanning mechanism allows the illumination and detection beam to

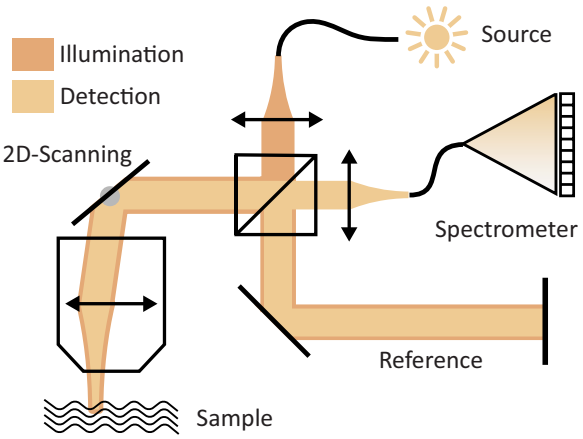

Fig. 1. (Color online) Layout of a spectrometer-based spectral domain OCT setup. Illumination and detection occurs through single mode fibers, and well defined illumination and detection modes. The free-space beam splitter decouples the detection from the illumination optics.

be scanned over the sample in both lateral directions. The incident light is scattered by the sample structure, and part of this light is collected by the sample objective. This sample light is recombined with the reference light at the beam splitter and coupled into the detection fiber. Both illumination and detection occur through single mode fibers and thus well defined illumination and detection modes. Fiber based systems, which use a fiber coupler to split and recombine the reference light in a Michelson configuration, use by definition the same optics for illumination and detection. A free-space beam splitter on the other hand offers the possibility to use different optics and define specific and distinct illumination and detection modes. Although more demanding in the alignment of the system, this decoupling of illumination and detection optics provides additional freedom in the system design and can be used to obtain improved imaging performance.

The interference signal coupled into the detection fiber is recorded as a function of its wavelength λ in the case of a spectrometer-based system. Remapping from λ to $k = 2\pi/\lambda$ provides the signal

$$P_{\mathrm{tot}}(k_p) = |S_{\mathrm{ref}}(k_p)|^2 + |S_s(k_p)|^2 + S_s(k_p)S_{\mathrm{ref}}^*(k_p) + S_s^*(k_p)S_{\mathrm{ref}}(k_p). \quad (1)$$

Without discussing the details of this crucial remapping, the signal is now given multiplexed into N wavenumber-channels, with k_p being the central wavenumber of the channel p, which has a narrow spectral width δk. To simplify the expressions, we approximate each wavenumber-channel as quasi-monochromatic, in which case the time dependence of the power signals drops out, and we write $P_{\mathrm{tot}}(k_p) = \langle P_{\mathrm{tot}}(t, k_p)\rangle$ to express the average power in the wavenumber-channel k_p. In this analytical notation, the signal generally comprises the independent terms from the reference and sample arms and two complex conjugate interference terms. Instead of recording the wavenumber-channels in parallel on a line camera, swept-source based systems acquire them over time, obtaining a similar signal. With dual balanced detection, the two independent terms are directly suppressed in this case. In spectrometer-based systems, the

term $|S_{\mathrm{ref}}|^2$ can in general be estimated by averaging of many acquisitions or prior recording. $|S_s|^2$ is much smaller than the reference signal and can be ignored. Many strategies to isolate a single one of the two complex conjugate signal terms exist [23–26]. In the simplest case the reference arm-length is adjusted to have a shorter reference path length than any signal from the sample arm to avoid the overlap of the conjugate terms. For the following we denote the term $P_s(k_p)=S_s(k_p)S^*_{\mathrm{ref}}(k_p)$ as the complex valued signal of FDOCM.

B. Generalized Aperture

First we would like to find expressions for the focal fields of the illumination and detection modes beyond the paraxial approximation, but considering scalar fields. This task has been widely studied, and the work of Gu [22] was closely followed. The interest here was to develop a signal model for FDOCT, where the dependence on the wavenumber of all expressions is crucial. Most of the literature on focal field calculations uses normalized coordinates and monochromatic waves, masking this dependence. For this reason we derive here the expression of the focal field for a general broadband light source.

As displayed in Fig. 2, the sample objective of focal length f is assumed to obey Abbe's sine condition and to perfectly focus an incident plane wave. It is characterized by a planar incident principal plane $\mathbf{P}_1$ and an object-side principal plane $\mathbf{P}_2$ of spherical shape. According to the Rayleigh–Sommerfeld diffraction integral, the field as a function of space and wavenumber at some point $\mathbf{r}$ in the focal volume can be expressed as a function of the field in the principal plane $\mathbf{P}_2$ of the objective as

$$\tilde{U}(\mathbf{r},k)=\frac{ik\,\exp(ikf)}{2\pi}\int_{\mathbf{P}_2}\tilde{U}(\mathbf{P}_2,k)\frac{\exp(-ikh)}{h}\cos(\mathbf{n},h)\mathrm{d}\sigma. \tag{2}$$

In the derivation of this expression from the Maxwell equations, monochromatic waves are usually considered. Time derivatives are trivial in that case and give rise to the ik factors in the above expression. If the field is written in a general manner in the spectral domain as a function of k, the time derivatives are still identical, and the same expression holds. The parameter k used in the above expression marks the difference to the quasi-monochromatic k_p used previously. The field $\tilde{U}(\mathbf{r},k)$ defines the field at a given point in space as a function of k, opposite to $U(\mathbf{r},k_p)$ that describes the time signal of a monochromatic field with wavenumber k_p in space. It would be more common to express the spectral envelope in terms of ω, with the Fourier transformation $\tilde{U}'(\omega)=\int U(t)\exp(-i\omega t)\mathrm{d}t$, indicated by the overtilde. To consistently evidence all $k=\omega/c$ factors, $\tilde{U}(k)=c\tilde{U}'(\omega)$ was used here.

As presented in Fig. 2, h is the distance between a point on the principal plane $\mathbf{P}_2$ and a point $\mathbf{r}$ within the focal volume, and $\mathbf{n}$ is the surface normal of $\mathbf{P}_2$. Given the geometry of the principal plane and if $f\gg|\mathbf{r}|$ it can be approximated that $\cos(\mathbf{n},h)\approx 1$. Within the Debye approximation $h-f\approx-\mathbf{r}\cdot\mathbf{p}$, where $\mathbf{p}$ is the unit vector pointing from the focal point toward $\mathbf{P}_2$. Using further $\mathrm{d}\sigma=f^2\mathrm{d}\Omega$, with Ω being the solid angle of the aperture, we find

$$\tilde{U}(\mathbf{r},k)=\frac{ikf}{2\pi}\int_{\mathbf{P}_2}\tilde{U}(\mathbf{p},k)\exp(ik\mathbf{p}\cdot\mathbf{r})\mathrm{d}\Omega. \tag{3}$$

To express the temporal evolution of the field in the general case of an arbitrary spectral envelope, the inverse transform $U(t)=1/(2\pi)\int\tilde{U}(k)\exp(ickt)\mathrm{d}k$ is computed as

$$U(\mathbf{r},t)=\frac{if}{4\pi^2}\int_k\int_{\mathbf{P}_2}\frac{\tilde{U}(\mathbf{p},k)}{k}\exp(ickt)\exp(ik\mathbf{p}\cdot\mathbf{r})k^2\mathrm{d}k\mathrm{d}\Omega. \tag{4}$$

An additional factor k was evidenced, and we are free to interpret the integral as a volume integral with the volume element $\mathrm{d}\mathbf{Q}=k^2\mathrm{d}k\mathrm{d}\Omega$. We define the three-dimensional vector $\mathbf{Q}$ with length $|\mathbf{Q}|=Q=k$ and orientation $\mathbf{Q}/Q=\mathbf{p}$. The focal field as a function of space $\mathbf{r}$ and

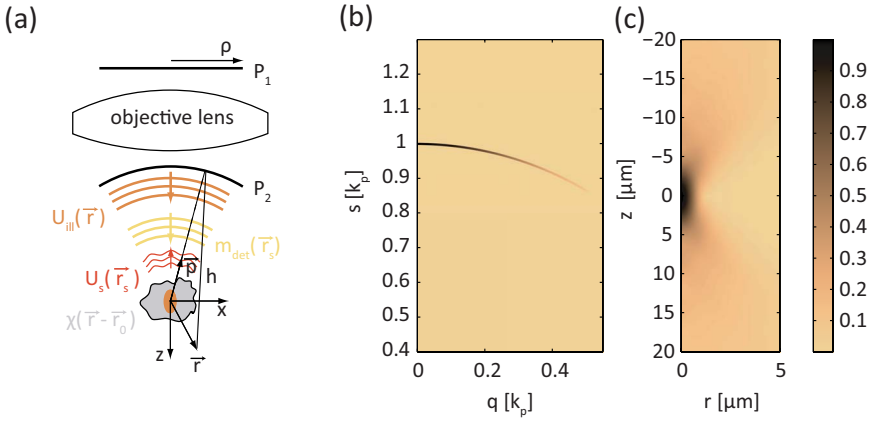

Fig. 2. (Color online) (a) Schematic of the situation at the sample objective. The field incident on the principal plane P_1 as a function of the radial coordinate ρ is transmitted by the objective to the principal plane P_2, which has the shape of a sphere cap. The illumination field U_{ill} is scattered by the susceptibility χ to produce the field U_s. Only its overlap with the detection mode m_{det} enters detection. (b) Principle of the generalized aperture. The plane wave components of the field in the focal plane are located in the spatial frequency domain on a sphere cap of radius k_p. The angular distribution of the amplitude on this sphere cap corresponds to the angular distribution in the sample objective's principal plane. (c) The three-dimensional Fourier transform of the generalized aperture produces the field in the focal region.

time t is now defined as the three-dimensional inverse Fourier transform of $\tilde{\tilde{U}}(\mathbf{Q})=2\pi f\tilde{U}(\mathbf{p},k)/k$, and we can identify $\mathbf{Q}$ as the three-dimensional spatial frequency. A factor of 2π was added to compensate for the $1/(8\pi^3)$ term in the Fourier transformation. The additional phase term adjusts the delay between the different spectral components:

$$U(\mathbf{r},t)=i\ \mathrm{FT}_{3D}^{-1}\{\tilde{\tilde{U}}(\mathbf{Q})\exp(icQt)\}. \tag{5}$$

For convenience we use for $U(\mathbf{r},t)$ the units of $\mathrm{W}^{1/2}\ \mathrm{m}^{-1}$, and accordingly we have $[\tilde{\tilde{U}}(\mathbf{Q})]=\mathrm{W}^{1/2}\ \mathrm{m}^2$. The formulation for a general field was necessary in order to evidence the integration along the wavenumber and to identify the volume integral $\mathrm{d}\mathbf{Q}$. Returning now to the monochromatic case of wavenumber k_p, the infinitesimally narrow spectral width defines in this case a spherical cap in the spatial frequency domain $\tilde{\tilde{U}}(\mathbf{Q})|_{k_p}=\tilde{\tilde{U}}(\mathbf{Q},k_p)=2\pi f\tilde{U}(\mathbf{p},k)\delta(Q-k_p)/Q$. The infinitely thin shell $\delta(Q-k_p)$ is usually referred to as the Ewald sphere. Dropping the harmonic time variation, we now can write

$$U(\mathbf{r},k_p)=i\ \mathrm{FT}_{3D}^{-1}\{\tilde{\tilde{U}}(\mathbf{Q},k_p)\},$$

$$\tilde{\tilde{U}}(\mathbf{Q},k_p)=-i\ \mathrm{FT}_{3D}\{U(\mathbf{r},k_p)\}. \tag{6}$$

This expression corresponds to McCutchen's generalized aperture [20]. The present derivation is however an important generalization, since it is valid for a field with an arbitrary spectral envelope with the monochromatic wave being simply a special case. The similarity between the spherical shell $\tilde{\tilde{U}}(\mathbf{Q},k_p)$ and the principal plane $\mathbf{P}_2$ of the sample objective is evident. Within the Debye approximation, the physical aperture is located in the far field of the focal volume, and hence the amplitude at a given location on this aperture contributes to the focal spot with a plane wave. This approximation is only valid in a confined region around the theoretical focus, but nevertheless also for very high NAs. The limitation to scalar waves and ignoring the polarization thus represent the most limiting assumption in the present formulation.

The re-interpretation of the field distribution in the objective principal plane as spatial frequency spectrum offers now a convenient way to compute the focal field in the sample volume for both the illumination and detection modes. The field as a function of ρ in $\mathbf{P}_1$ can safely be calculated with paraxial optics approximations, defined by the illumination and detection optics. For the moment a collimated Gaussian beam with $1/e^2$ intensity waist ω_0 is assumed to illuminate the backaperture of the sample objective that has a circular aperture of radius ρ_0. The objective's NA is taken as $\mathrm{NA}=\rho_0/f$. The Gaussian beam is thus truncated, characterized by the truncation parameter $\kappa=\omega_0/\rho_0$. The waist is taken to be independent of the wavenumber k_p. This situation is more or less achieved when broadband light is delivered through a single mode fiber and collimated with an achromatic lens. Since the fiber mode diameter scales roughly with the wavelength, the collimated beam, which corresponds to the far field pattern of the fiber mode, is approximately constant for different k_p's. With the sine condition as the apodization function $f\sin\theta=\rho$ and the incoming field is scaled with a term $\cos^{1/2}\theta=(s/Q)^{1/2}$, $\tilde{U}^{P_2}(fq/Q)=\tilde{U}^{P_1}(fq/Q)(s/Q)^{1/2}$. It is now possible to construct the generalized aperture:

$$\tilde{\tilde{U}}(\mathbf{Q},k_p)=2\pi f\tilde{U}^{P_2}\left(f\frac{q}{Q}\right)\frac{\delta(Q-k_p)}{Q}, \tag{7}$$

where the field $\tilde{U}$ in $\mathbf{P}_1,\mathbf{P}_2$ is given in $\mathrm{W}^{1/2}$. We use $\mathbf{Q}=q_x\mathbf{e}_1+q_y\mathbf{e}_2+s\mathbf{e}_3$, with $\mathbf{e}_i$ being the unit vectors of an orthonormal basis, $\mathbf{q}=q_x\mathbf{e}_1+q_y\mathbf{e}_2$, and $q=|\mathbf{q}|$.

Figure 2(b) shows the generalized aperture for an objective with a NA of 0.5 and $\kappa=0.7$. For the numerical implementation, the Dirac expression was approximated with a Gaussian envelope of width $\delta k=k_p/150$. Assuming circular symmetry around s, the generalized aperture is displayed as a function of the axial spatial frequency s and the lateral component q. Computing the three-dimensional inverse Fourier transformation, the field in the focal volume is found as depicted in Fig. 2(c). To simplify and accelerate this computation, and using the circular symmetry of the expression, an implementation of the fast Hankel transform along q and the chirped z-transform along s were used.

C. Scattered Field

With the illumination and detection modes in the focal volume known, the interaction with the sample is now considered. According to the first order Born approximation and for scalar waves, the field scattered by a sample inhomogeneity at the quasi-monochromatic wavenumber k_p expressed on a surface lying outside the inhomogeneity and parameterized by $\mathbf{r}_s$ is

$$U_s(\mathbf{r}_s,\mathbf{r}_0,k_p)=\frac{k_p^2}{4\pi}\int_V U_{\mathrm{ill}}(\mathbf{r},k_p)\chi(\mathbf{r}-\mathbf{r}_0)\frac{\exp(-ik_p|\mathbf{r}_s-\mathbf{r}|)}{|\mathbf{r}_s-\mathbf{r}|}\mathrm{d}V. \tag{8}$$

Here $\chi(\mathbf{r})=n^2(\mathbf{r})-1$ is the sample susceptibility, and $\mathbf{r}_0$ defines the position of this sample structure with respect to the illumination field. The scanning mechanism varies $\mathbf{r}_0$, either by redirecting the beam to another point on the sample or by physically moving the sample with respect to the beam. The often used scattering potential $F(\mathbf{r},k)=k^2\chi(\mathbf{r})/(4\pi)$ depends explicitly on the wavenumber k. To keep track of all wavelength dependent variables, here the susceptibility was chosen instead to express the sample structure. It is assumed to be non-dispersive and hence independent of k.

The discussed situation is outlined in Fig. 2(a). To quantify the amount of the scattered field collected by the detection optics, the mode overlap between the scattered field and the detection mode is computed. For this procedure, the principal plane $\mathbf{P}_2$ on the object side of the sample objective is chosen. Both the spatial and frequency modes have to match to assure coupling. Since we stipulated a set of discrete wavenumber modes the amount of the field scattered at a given wavenumber coupled into its corresponding wavenumber-channel becomes

$$S_s(r_0,k_p)=\int_{\mathbf{P}_2} U_s(r_s,r_0,k_p)m_{\mathrm{det}}(r_s,k_p)\mathrm{d}\sigma, \tag{9}$$

in the space-time coordinate system, where the mode m_{det} was defined in units of 1/m, yielding $[S_s]=\mathrm{W}^{1/2}$.

The scattered field U_s is propagating away from the focal volume. The portion of interest propagates along the negative z direction toward the detection optics. The detection mode m_{det} on the other hand was deliberately defined as propagating in parallel with the illumination mode in the positive z direction. This definition corresponds to the mode that would be produced if the sample was illuminated through the detection fiber. The true detection mode however propagates in the opposite direction. In the overlap integral the target mode usually appears in its complex conjugated form. Since taking the complex conjugate is equivalent for a monochromatic wave to a change of the direction of propagation, the complex conjugate could be omitted with the present definition of m_{det}.

D. Coherent Transfer Function

Based on the former analysis, we can recast expression (9) in a more complete form. Combining Eqs. (8) and (9) and inverting the order of integration produces

$$S_s(\mathbf{r}_0,k_p)=\frac{k_p^2}{4\pi}\int_V U_{\mathrm{ill}}(\mathbf{r},k_p)\chi(\mathbf{r}-\mathbf{r}_0)\times\int_{\mathbf{P}_2} m_{\mathrm{det}}(\mathbf{r}_s,k_p)\frac{\exp(-ik_p|\mathbf{r}_s-\mathbf{r}|)}{|\mathbf{r}_s-\mathbf{r}|}\mathrm{d}\sigma\mathrm{d}V. \tag{10}$$

Comparing the inner integral of this result with Eqs. (2) and (3), taken for the monochromatic case, we find

$$\int_{\mathbf{P}_2} m_{\mathrm{det}}(\mathbf{r}_s,k_p)\frac{\exp(-ik_p|\mathbf{r}_s-\mathbf{r}|)}{|\mathbf{r}_s-\mathbf{r}|}\mathrm{d}\sigma \approx \frac{-i2\pi\exp(-ik_pf)}{k_p}m_{\mathrm{det}}(\mathbf{r},k_p), \tag{11}$$

and, hence, ignoring the phase term $\exp(-ik_pf)$,

$$S_s(\mathbf{r}_0,k_p)=\frac{-ik_p}{2}\int_V U_{\mathrm{ill}}(\mathbf{r},k_p)m_{\mathrm{det}}(\mathbf{r},k_p)\chi(\mathbf{r}-\mathbf{r}_0)\mathrm{d}V. \tag{12}$$

The signal coupled into the detection fiber is expressed as the product of the illumination field and the detection mode, convolved with the sample structure according to the scanning $\mathbf{r}_0$. The illumination field can be separated into the illumination mode $U_{\mathrm{ill}}(\mathbf{r},k_p)=\tilde{A}^{1/2}(k_p)m_{\mathrm{ill}}(\mathbf{r},k_p)$ with $[m_{\mathrm{ill}}]=[m_{\mathrm{det}}]=1/\mathrm{m}$ and the spectral envelope $\tilde{A}(k_p)$, defining the power in each wavenumber-channel.

Taking into account the reference amplitude $S_{\mathrm{ref}}^*=\tilde{A}^{1/2}(k_p)$ the signal $P_s(\mathbf{r}_0,k_p)=S_sS_{\mathrm{ref}}^*$ can now be expressed. With a complete three-dimensional scan $\mathbf{r}_0$, as performed in confocal microscopy, the recorded signal could be Fourier transformed to the spatial frequency domain along all three spatial coordinates. Since in the spatial coordinates the sample structure was convolved with the product of the illumination and the detection mode, in the spatial frequency domain, this translates into the product of the sample spectrum with the convolution of the illumination and detection generalized apertures, obtained by transformation according to Eq. (6):

$$\tilde{\tilde{P}}_s(\mathbf{q},s,k_p)=\frac{ik_p\tilde{A}(k_p)}{2}[\tilde{\tilde{m}}_{\mathrm{ill}}(\mathbf{q},s,k_p)\otimes\tilde{\tilde{m}}_{\mathrm{det}}(\mathbf{q},s,k_p)]\tilde{\tilde{\chi}}(\mathbf{q},s)$$
$$=ik_p\tilde{A}(k_p)\mathrm{CTF}(\mathbf{q},s,k_p)\tilde{\tilde{\chi}}(\mathbf{q},s). \tag{13}$$

The convolution of the two sphere caps defined by the generalized apertures leads to the three-dimensional coherent transfer function $\mathrm{CTF}=1/2\tilde{\tilde{m}}_{\mathrm{ill}}\otimes\tilde{\tilde{m}}_{\mathrm{det}}$, which has the unit of meters here. In the case of three-dimensional scanning the signal recorded in an individual wavenumber-channel indeed leads to a linear filtering process, with the CTF defining the filter in the spatial frequency domain. This powerful concept was mainly promoted by Sheppard *et al.* [21]. The present derivation follows closely their work, but emphasizes the importance of the wavenumber k_p to arrive at a meaningful expression for the FDOCM signal.

To evaluate the CTF, by geometrical considerations, as depicted in Fig. 3, the intersection of the two spherical

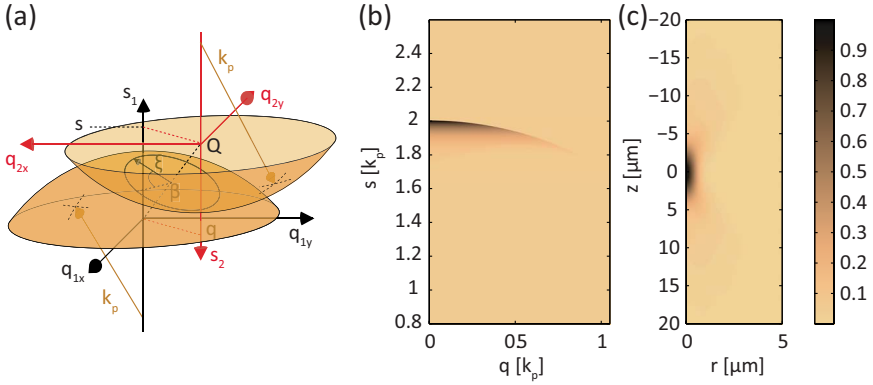

Fig. 3. (Color online) (a) Schematic of the convolution of two spherical shells, creating a circular overlap region. (b) CTF for identical generalized apertures with Gaussian modes and NA=0.5 and $\kappa=0.7$. (c) The three-dimensional inverse Fourier transformation of the CTF produces the PSF ($k_p=2\pi/\lambda_p$ and $\lambda_p=780$ nm).

shells, offset by $\mathbf{Q}=(\mathbf{q},s)$, is identified as a circle with radius $\xi=(k_p^2-Q^2/4)^{1/2}$. To compute the convolution at a given point $\mathbf{Q}$ it is sufficient to evaluate the integral along this line, although the surface element $\Delta\sigma(\mathbf{q},s)$ of the cross-section of the cap intersection volume has to be considered. Although the sphere caps are infinitesimally thin here, it can be shown by computing the precise overlap volume between two shells of decreasing thicknesses that a correction term $\Delta\sigma(\mathbf{q},s)=k_p^2/(\xi Q)$ remains. Substituting from Eq. (7) and using the fact that on the intersection circle by definition $Q_1=Q_2=k_p$, we obtain

$$\mathrm{CTF}(q,s)=4\pi^2f^2\int_{\beta_i}^{\beta_e}\tilde{m}_{\mathrm{ill}}^{P_2}\left(f\frac{q_1}{k_p}\right)\tilde{m}_{\mathrm{det}}^{P_2}\left(f\frac{q_2}{k_p}\right)\frac{\xi\Delta\sigma}{k_p^2}\mathrm{d}\beta$$
$$=\frac{4\pi^2f^2}{Q}\int_{\beta_i}^{\beta_e}\tilde{m}_{\mathrm{ill}}^{P_2}\left(f\frac{q_1}{k_p}\right)\tilde{m}_{\mathrm{det}}^{P_2}\left(f\frac{q_2}{k_p}\right)\mathrm{d}\beta, \quad (14)$$

where q_1 and q_2 are functions of β, used to parameterize the intersection circle. Decoupled and distinct illumination and detection apertures are considered here. Since both modes travel through the same objective, identical NAs are however assumed, and the integral is taken twice from $\beta_i=-\pi/2$ to $\beta_e=\pi/2$ if $s/2>\xi q/Q+k_p(1-\mathrm{NA}^2)^{1/2}$ and $\beta_{i/e}=\mp\sin^{-1}[Q(s/2-k_p(1-\mathrm{NA}^2)^{1/2})/(\xi q)]$, otherwise.

For numerical evaluation, it is more convenient to evaluate the integral as a function of s_1. Performing a change of variable where $\beta=\sin^{-1}[Q(s_1-s/2)/(\xi q)]$ and using $\tilde{m}_{\mathrm{ill/det}}(s)=\tilde{m}_{\mathrm{ill/det}}^{P_2}(f(1-s_{1/2}^2/k_p^2)^{1/2})=\tilde{m}_{\mathrm{ill/det}}^{P_1}(f(1-s_{1/2}^2/k_p^2)^{1/2})(s_{1/2}/Q_{1/2})^{1/2}$ leads to

$$\mathrm{CTF}(q,s)=\frac{4\pi^2f^2}{Q}\int_{s_{1i}}^{s_{1e}}\tilde{m}_{\mathrm{ill}}(s_1)\tilde{m}_{\mathrm{det}}(s-s_1)$$
$$\times\frac{\mathrm{d}s_1}{\sqrt{\frac{\xi^2q^2}{Q^2}-\left(s_1-\frac{s}{2}\right)^2}}. \quad (15)$$

Here, $s_i=k_p(1-\mathrm{NA}^2)^{1/2}$ and $s_e=s-s_i$ if $s<k_p+k_p(1-\mathrm{NA}^2)^{1/2}$, and $s_i=s-k_p$ and $s_e=k_p$, otherwise. The CTF can be interpreted as the convolution of the illumination and detection generalized apertures as a function of their axial spatial frequencies, in the presence of an additional Kernel that depends on q, s, and s_1. For numerical implementation the modes are discretized at the points $s[n]=2k_p(1-\mathrm{NA}^2)^{1/2}+n\Delta s$, $s_1[j]=k_p(1-\mathrm{NA}^2)^{1/2}+j\Delta s$, with $\Delta s=2k_p(1-(1-\mathrm{NA}^2)^{1/2})/(N-1)$ and $n\in[0,N-1]$, $j\in[0,N/2-1]$. The lateral spatial frequency is represented as $q=m\Delta q$, with $\Delta q=2k_p\mathrm{NA}/(M-1)$, $q\in[0,M-1]$. To circumvent the singularity in the Kernel, it is integrated analytically, and the expression for the CTF at a given discretized spatial frequency n,m becomes, for $m>0$,

$$\mathrm{CTF}[n,m]=\frac{4\pi^2f^2}{Q}\sum_{j=a}^{b}\tilde{m}_{\mathrm{ill}}[j]\tilde{m}_{\mathrm{det}}[n-j](W_+[n,m,j]$$
$$-W_-[n,m,j]), \quad (16)$$

where

$$W_\pm[n,m,j]=\sin^{-1}\left(\frac{Q[n,m]\left(s[j]\pm\frac{\Delta s}{2}-\frac{s[n]}{2}\right)}{q[m]\xi[n,m]}\right), \quad (17)$$

and $a=0$, $b=n$ for $n\le N/2-1$ and $a=N-n$, $b=N/2-1$ for $n>N/2-1$. For the case $m=0$, $\mathrm{CTF}[n,m=0]=(8\pi^3f^2/Q)\tilde{m}_{\mathrm{ill}}(s[n]/2)\tilde{m}_{\mathrm{det}}(s[n]/2)$.

Although the arcsine computations are computationally rather costly, this expression can be evaluated numerically. Figure 3 displays the result for the case of illumination and detection apertures, which are both identical to the aperture illuminated with a Gaussian beam used previously (cf. Fig. 2). Here, $N=2048$ and $M=1024$, and the computation with a 2.13 GHz dual core Intel Xeon based personal computer with 4 Gbytes DDRII SDRAM took approximately 10 min.

Despite the infinitesimally thin sphere caps of the generalized apertures, the CTF gives rise to nonzero transmission coefficients within a volume in the three-dimensional spatial frequency domain. The CTF describes the spatial frequencies of the sample susceptibility that can be accessed by measuring the scattered field in a confocal imaging system at a monochromatic wavelength k_p. The convolution of the generalized apertures has increased the axial and lateral support by a factor of 2 compared to the initial apertures in the presented case. The support in each direction defines the resolution in the corresponding spatial coordinate, evidencing the resolution advantage of a confocal setting compared to a wide field configuration. While the transmission profile for lateral spatial frequencies is of a low-pass type, in reflection mode, axial spatial frequencies are transmitted within a bandpass window.

E. FDOCM Signal

The motivation of spectral domain OCT is to retrieve the sample structure along depth in parallel without axial scanning. Looking at the FDOCM system as a wavenumber multiplexed interference microscope, each wavenumber-channel has its own specific CTF. Figure 4(a) shows the CTFs of three different wavenumbers $k_c-\Delta k_{\mathrm{FWHM}}/2$, k_c, and $k_c+\Delta k_{\mathrm{FWHM}}/2$, with $\Delta k_{\mathrm{FWHM}}=k_c/5$ and k_c being the central wavenumber. The CTFs of the different wavenumbers are similar and have a point symmetry about the origin with additional amplitude scaling by $1/k_p$. As seen in Fig. 4(b), this scaling normalizes the integral $\int\mathrm{CTF}(\mathbf{q},s,k_p)\mathrm{d}s$, since the support increases with k_p at the same time as the amplitude decreases with its inverse.

The CTF defines which spatial frequencies of the sample can be assessed by a specific wavenumber-channel. But in order to retrieve the spatial sample information, the sample also has to be sampled correctly. The sampling points in the spatial frequency spectrum are defined through the discrete spatial sampling steps of the confocal setup. Only when the Nyquist frequency is respected can the spatial frequency information indeed be retrieved. While the sample is scanned in the lateral direction in spectral domain OCT, the axial direction is omitted, and the information along the axial spatial frequency within the CTF is not captured. A two-

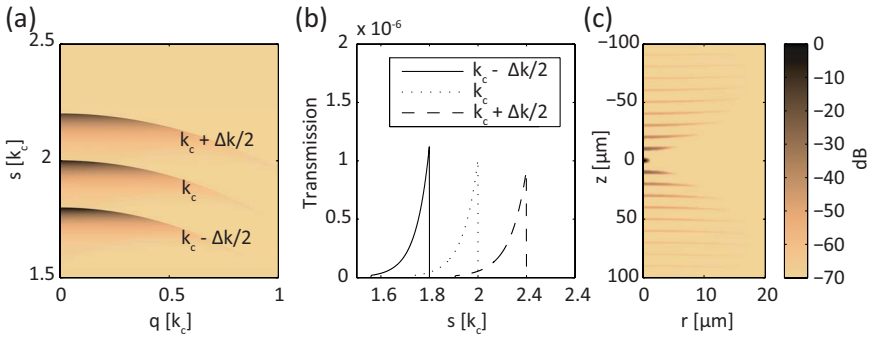

Fig. 4. (Color online) (a) CTF for Gaussian illumination with NA=0.5 and $\kappa=0.7$ for three different wavenumbers. (b) Plot of the same three CTFs shown in (a), at $q=0$, evidencing the scaling of the CTF with k_p. The amplitude decreases along with an scaling of the support length, making the integral of the CTF along s at $q=0$ constant. (c) Simulated tomogram of idealized scatterers, aligned along the optical axis spaced by 10 μm in logarithmic scale ($k_p=2\pi/\lambda_p$ and $\lambda_p=780$ nm, $\Delta k_{\mathrm{FWHM}}=k_c/5$).

dimensional signal is recorded for each spectral channel. In the spatial frequency domain this corresponds to taking the projection of the product of the sample structure and the CTF along s, which is equivalent to the confocal signal at $z=0$,

$$\tilde{P}_s(\mathbf{q},k_p)|_{z=0} = ik_p\tilde{A}(k_p)\int_s \mathrm{CTF}(\mathbf{q},s,k_p)\tilde{\tilde{\chi}}(\mathbf{q},s)\mathrm{d}s. \quad (18)$$

Instead of using axial scanning to access the axial spatial frequencies, spectral domain OCT uses the fact that the CTFs of the wavenumber-channels occupy each a distinct volume in the spatial frequency domain. Although the axial information within an individual channel is not resolved, the combination of signals from all the channels gives access to the axial spatial frequencies in the range of the system's CTFs at the accessible source wavelengths.

For this spatial frequency sampling to work correctly, the support along s of the CTFs should be as short as possible. As discussed, they extend however over a finite range along s, and the CTFs of neighboring wavenumber-channels overlap, which confuses the correct sampling of the sample information.

The classical way to reconstruct the tomogram is to take the inverse Fourier transformation of $\tilde{P}_s(\mathbf{q},\mathbf{r})$ from k_p to z. Taking into account the scaling of the z-coordinate by a factor of 2, the tomogram becomes

$$\begin{aligned} T(\mathbf{q},z) &= \int_{k_p} \tilde{P}_s(\mathbf{q},k_p)\exp(i2k_pz)\mathrm{d}k_p \\ &= i\int_{k_p} k_p\tilde{A}(k_p)\int_s \tilde{\tilde{\chi}}(\mathbf{q},s)\mathrm{CTF}(\mathbf{q},s,k_p)\mathrm{d}s \\ &\quad \times\exp(i2k_pz)\mathrm{d}k_p. \end{aligned} \quad (19)$$

In this general form it is difficult to further simplify the expression. If it was assumed that the CTF would not scale with k_p but merely shift along s, one could write $\mathrm{CTF}(\mathbf{q},s,k_p)=\mathrm{CTF}(\mathbf{q},s,k_c)\otimes\delta(k_p-k_c)=\mathrm{CTF}(\mathbf{q},s-2(k_p-k_c))$ and identify the inner integral as the convolution of the sample spectrum with the CTF. In this case

$$T(\mathbf{q},z) = A'(z)\otimes[\widetilde{\mathrm{CTF}}(\mathbf{q},z)\tilde{\chi}(\mathbf{q},z)]. \quad (20)$$

Here, $A'(z)=\int ik_p\tilde{A}(k_p)\exp(i2k_pz)\mathrm{d}k_p \approx i2k_cA(z)\times\exp(i2k_cz)$ defines the axial resolution of the system, according to the spectral width of the light source. In this form, the additional factor ik_p differentiates the classical coherence gate $A(z)=\int\tilde{A}(k_p)\exp(i2k_pz)\mathrm{d}k_p$. The effect of this derivation is however negligible since the Gaussian spectrum is centered at k_c. The exponential term $\exp(i2k_cz)$ acts as a high-pass filter.

The action of the CTF in this representation is now disclosed: after transformation from s to z it imposes an axial envelope, defining an axial range within which the signal has appreciable values, and contributes to the DOF. The length of this envelope is inversely proportional to the width of the CTF support along s. This effect is independent of the defocusing, which only comes into play in the spatial coordinates after transformation of the above expressions from $\mathbf{q}$ to $\mathbf{r}$, and will be analyzed in the next section. The physical meaning of the reconstructed tomogram is also revealed: the signal is indeed proportional to the high-pass filtered sample susceptibility, thus evidencing mainly the variations in the squared refractive index.

A further approximation for the CTF can be taken in the case of very small NAs. In this situation, the support of the CTF along the axial spatial frequency becomes negligibly small and can be approximated as $\mathrm{CTF}(\mathbf{q},s,k_p)=\mathrm{CTF}'(\mathbf{q})\delta(s-2k_p)$. Equation (19) simplifies in this case to

$$T(\mathbf{q},z) = i\int_{k_p} k_p\tilde{A}(k_p)\mathrm{CTF}'(\mathbf{q})\tilde{\tilde{\chi}}(\mathbf{q},2k_p)\exp(i2k_pz)\mathrm{d}k_p. \quad (21)$$

The tomogram can be described as a linear filtering now. The lateral support of the filter is defined by the CTF and the axial extent by the spectrum of the employed light source, as described by Coupland [19]. In the general case, however, and especially for higher NAs, this approximation cannot be taken since the width along s of the CTFs increases $\propto\mathrm{NA}^2$, whereas the lateral width progresses only linearly with the NA.

3. SIMULATION

To investigate the various effects and limitations imposed by the CTF, we take idealized point-like scatterers

aligned along the z-axis as a sample structure to compute numerically the expected tomogram

$$\tilde{\tilde{\chi}}(\mathbf{q},s) = \int \sum_n \delta(z - n\Delta z)\exp(-i\mathbf{Q}\cdot\mathbf{r})\mathrm{d}\mathbf{Q} = \sum_n \exp(-isn\Delta z). \tag{22}$$

Computing expression (19) with this sample structure corresponds to taking the Fourier transformation of the CTF at given z-positions and for each wavenumber k_p. In practice this was achieved efficiently using the chirped z-transform, which allowed using a single computation of the CTF and subsequent scaling of the support vectors. After multiplication with $k_p\tilde{A}(k_p)$ and consequent Fourier transformation the simulated tomogram was obtained. For the simulation, $k_c = 2\pi/\lambda_c$ was set to $\lambda_c = 780$ nm, $\Delta k_{\mathrm{FWHM}} = k_c/5$ unless otherwise stated, and the whole k-support of 2048 wavenumber-channels spanned a range of 3.5 times Δk_{FWHM} to avoid ringing. The specified NAs express directly the opening angle of the objective, assuming an objective without immersion.

Figure 4(c) shows the result for the case of the previously described Gaussian optics with NA=0.5. The very short DOF is obvious, and outside the focal plane the signal is severely blurred and reduced in amplitude. The tomogram is plotted in the logarithmic scale, taking $20\log_{10}(T(\mathbf{r},z))$.

In order to gain further insight into the mechanisms that degrade the tomogram and define the short DOF, we constructed hypothetical CTFs, which—although synthetic—help to understand the underlying principles. All the CTFs at a given NA were matched to have an in-focus resolution identical to the Gaussian case of the same NA. For this, the projections of the CTFs along s were matched to the Gaussian CTF. Three different CTFs were constructed and are presented in Fig. 5 for NA=0.5. Based on the CTFs, the corresponding tomograms were computed, again by taking into account the scaling of the CTF with k_p and its point symmetry about the origin.

In the first case [Fig. 5(a)], the CTF was defined with a very narrow envelope along s, separable from its q-dependence which was matched to the Gaussian CTF. The tomogram in Fig. 5(d) is nearly ideal with an unaltered lateral resolution and a nearly constant signal amplitude over the considered depth range. The short s-support avoids confusion of the spatial frequency sampling by the different wavenumbers, and the Fourier transformation of the short s-support produces a very large z-envelope. This situation would result in a near-linear filtering, analogous to a very low NA system, as discussed before.

The second CTF [Figs. 5(b) and 5(e)] likewise features separable q and s-envelopes. In this case, the axial envelope was however matched to the Gaussian case CTF($\mathbf{q}=0,s$). Here, the large support along s defines a very short axial envelope, suppressing the signal outside the focal plane. Still, the lateral resolution remains invariant as a function of depth, as in the previous case.

While the width of the CTF along the axial spatial frequency imposes an amplitude envelope, it does not affect the lateral resolution. The lateral blurring of the signal is induced by the defocusing, which originates in the curvature of the CTF. Figures 5(c) and 5(f) display the CTF and the tomogram for a CTF with still the same lateral envelope, but a support that defines a sphere cap with radius $2k_p$, analogous to the curvature of the Gaussian CTF. There are no longer separable envelopes along $\mathbf{q}$ and s in this case. The resulting tomogram is marked by a clearly defined short DOF, outside of which the scatterer signals are severely blurred.

Indeed, the short width along s correctly samples the spatial frequencies without confusion and without imposing an axial amplitude envelope. However, the position of the albeit very short CTF support is shifted along s as a function of q according to the CTF curvature. But for FDOCT's reconstruction algorithm to work correctly, the CTF should sample a single axial spatial frequency s in a given wavenumber-channel. Representing the tomogram in the lateral spatial frequencies, $T(\mathbf{q},z)$, the effect of the defocusing is not yet manifest, and the signal indeed extends over a long axial range for the discussed CTF. But according to the sifting-theorem, the CTF's curvature introduced a phase offset as a function of $\mathbf{q}$ upon transformation from s to z. After the transformation from $\mathbf{q}$ to the spatial domain $\mathbf{r}$ the various spatial frequency components add up constructively only in the focal plane, where

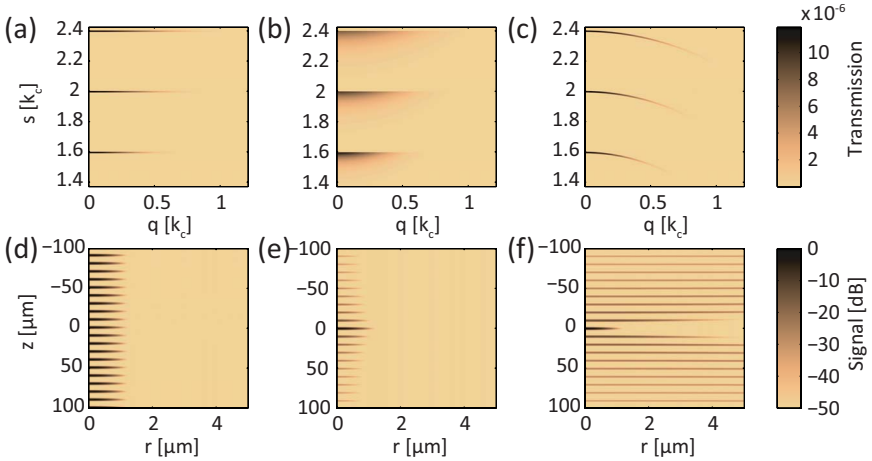

Fig. 5. (Color online) (a) Ideal CTF with very short support along s and no curvature. (b) Broad CTF, with separable q and s envelopes. (c) Cap CTF, with short s support, but curvature of radius $2k_p$. (d), (e), (f) Tomograms produced with CTFs in (a), (b), and (c), respectively.

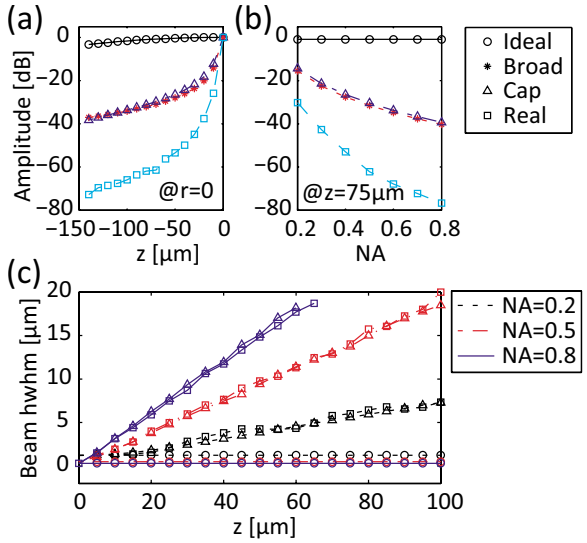

Fig. 6. (Color online) (a) Signal amplitude of idealized scatterers, positioned on the optical axis as a function of the out-of-focus distance, for the three idealized configurations presented in Fig. 5 and the realistic case in Fig. 4 at NA=0.5. (b) Signal amplitude at a given out-of-focus distance of 75 μm for the same configurations as in (a), but with varying NA. (c) hwhm of the scatterer signals for several configurations as a function of the out-of-focus distance.

the phase offset is zero, and define a diffraction limited spot. But outside the focal plane the introduced phase variation blurs the signal heavily.

Figure 6 compares the synthetic configurations with the simulation of the realistic Gaussian-like scenario. The signal amplitude of the point-like scatterers as a function of z reveals that the defocusing effect and the amplitude envelope imposed by the width of the s-support contribute equally to the extent of the DOF. The observed DOF in the realistic scenario is the product of both the transform limitation of the axial envelope and the defocusing. Figure 6(b) displays the signal amplitude at 75 μm from the focal plane as a function of the NA. The NA of the Gaussian case was varied, keeping κ constant, and for each Gaussian template-CTF the synthetic versions were derived. Independent of the NA, the contribution of the transform limitation and the defocusing remains equal. In Fig. 6(c) we extracted the lateral half-width at half-maximum (hwhm) of the lateral spots by tracking the axial local signal maximum, starting at $\mathbf{r}=0$. The blurring for the realistic and the sphere cap CTF are identical, while the CTFs with separable $\mathbf{q}$ and s variables produce no defocusing at all.

So far, all the simulations took the scaling of the CTF with k_p into account. As well the widths of the lateral $\mathbf{q}$- and the axial s-support increase with k_p, in hand with a decrease in the transmission amplitude. The approximated situation of a constant CTF simply shifting along s would result, by using Eq. (20), the definition of the probing sample [Eq. (22)], and the associativity of the convolution, in

$$T(\mathbf{r},z) = \mathrm{PSF}(\mathbf{r},z)\left[A'(z) \otimes \sum_n \delta(z - n\Delta z)\right]. \qquad (23)$$

In this case, a point-spread function (PSF) can be evidenced and is directly given by the transform of the CTF, $\mathrm{PSF}(\mathbf{r},z) = \int \mathrm{CTF}(\mathbf{Q},k_c)\exp(i\mathbf{Q}\cdot\mathbf{r})\mathrm{d}\mathbf{Q}$, defining the lateral blurring of the scatterers independent of the spectral width of the light source. The axial position on the other hand is revealed by the spectral interference pattern. An out-of-focus scatterer becomes in this approximation a flat disk, with its radius defined by the width of the PSF and the thickness by the coherence gate. As noticed before and shown in Fig. 7 in detail, the scaling of the CTF with k_p results in a curving of the out-of-focus scatterer image. The coherence gate locates signals according to their group delay. Because the outer shell radius of the CTF changes as a function of k_p, the resulting group delay is a function of the lateral position of the scattering particle, and contrary to the approximated model of a constant CTF, the tomogram of the scanned particle is no longer located on a plane $z=$const, but on a curved surface.

Despite its limitation, it might still be very attractive to judge on the expected DOF and lateral resolution of the system based on this simplified model, since the simulation of the tomogram of the scatterers is by far less complex in this case. To further investigate the limitations and accuracy of the simplified model, Fig. 7(b) compares the signal amplitude of the simulated scatterers with the envelope defined by the direct transformation of the central wavenumber's CTF. The simplified model very accurately predicts the signal amplitude, and can thus be used to judge on the available DOF. Even with increasing spectral width of the light source, the amplitude of the scat-

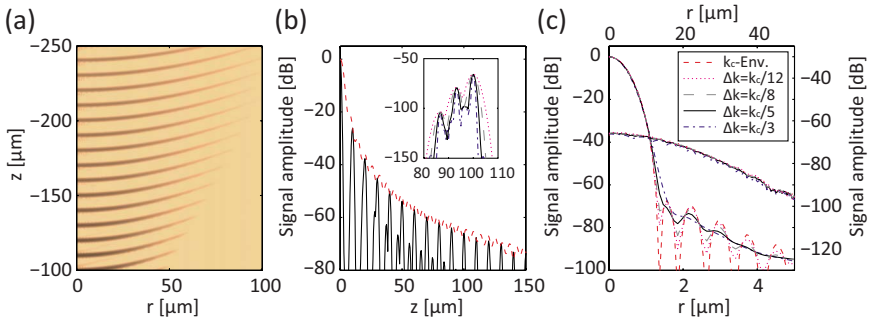

Fig. 7. (Color online) (a) Detailed view of out-of-focus scatterers for NA=0.5 evidencing the axial curvature of the signal in the tomogram. (b) Comparison of the axial signal amplitude of the simulated scatterers with the envelope imposed by the PSF of the central wavenumber. Inset: Detailed view of the peak splitting of the scattering signal for various spectral widths. (c) Scattering signal in the lateral direction for the in-focus and out-of-focus ($z=50$ μm) situations, for the accurate model simulation and the direct PSF prediction. The legend applies to both (b) and (c).

tering signal on the axis is unaltered. In the accurate model, however, the increasing bandwidth induces further artifacts, resulting in a peak splitting of the out-of-focus scatterers as indicated in the inset in Fig. 7(b). Despite this effect, the lateral definition, obtained by tracking the peak maximum in the lateral direction along its curved shape, corresponds well to the value predicted by the simplified model. The scaling with k_p smooths however the lateral signal envelope. At a given wavenumber the PSF might exhibit a zero in the field amplitude at a certain radial position. But this position is a function of k_p, and thus averaged in the tomogram signal of the accurate model. The effect on the hwhm of the signal peak can meanwhile be safely ignored.

Despite all these effects, for the spectral bandwidths of most light sources, $\Delta k < k_c$ holds, and the on axis amplitude of the signal peaks is accurately predicted by the transform of the central wavenumber's CTF($\mathbf{q}, s, k_c$), as if the scaling of the CTF with k_p was ignored. This is an important finding since computing the CTF for the central wavenumber as a function of the system parameters and its transformation to spatial coordinates allows one to judge accurately on the expected DOF, limited by both the defocusing and the axial envelope.

4. DISCUSSION

Using theoretical tools developed for conventional microscopy, we have proposed a model providing a description of the signal recorded by FDOCM and the reconstructed tomogram. The image formation in confocal microscopy, obtained by three-dimensional scanning, can be expressed as a linear filtering process where the scan in each direction results in the convolution of the sample structure with the PSF, i.e., the sample spectrum is filtered by the system transfer function. FDOCM, on the other hand, replaces the axial third scan with the multiplexed detection. Ideally, FDOCM should measure $\tilde{\tilde{\chi}}(\mathbf{q}, s)$. The recorded signal however provides $\tilde{P}_s(\mathbf{q}, k_p)$ [Eq. (18)]. Instead of sampling the spatial frequency spectrum on a regular grid in the $\mathbf{q}, s$-domain, the sampling occurs as a function of the wavenumber-channel's specific CTFs.

The CTF defines which spatial frequencies of the sample are accessible by a given wavenumber-channel, and it spans a volume in the spatial frequency domain. The width of this support in the lateral direction defines the lateral resolution. Importantly, the exact amplitude envelope of the CTF also influences the final lateral PSF. For the Gaussian-like illumination, this envelope indeed features a very smooth shape, but when distinct illumination and detection apertures are combined, this is not necessarily the case. The essential finding of this work is that both the curvature of the CTF and its width along s contribute to the limitation of the DOF with two fundamentally different mechanisms. As a function of depth, the curvature induces a defocusing due to a pure phase offset of the various lateral spatial frequency components. The signal energy is not reduced in this case but simply blurred laterally. However, if the axial width of the CTF becomes significant compared to the wavenumber-channel spacing, the spatial frequency information becomes increasingly confused, leading to reduced signal energy.

In the spatial domain, the physical setting seems more intuitive at first. The illumination and detection optics create a specific focal volume, i.e., PSF, with a characteristic DOF. Since scanning is performed only in the lateral directions, the sample structure lying outside the focal plane is blurred. Instead of leaving a diffraction limited spot, the trace of a single scatterer now extends over a larger area. But integrating the energy of this spread does not amount to the same value as in the case of the in-focus situation, because at each scanning position, the particle has only received a small fraction of the illumination power. Correspondingly, the backscattered photons were also detected with a lower efficiency as compared to the in-focal plane, leading to the observed axial amplitude envelope. Whereas these two effects are inherently linked in the spatial domain, the representation in the spatial frequency domain separates them into two independent mechanisms.

The view in the spatial domain becomes increasingly complicated if it is considered that the focal volume depends on the wavelength and that the phase-fronts away from the focal volume are curved. Furthermore, the focal volume in OCT is most often considered as being Gaussian. This is a safe assumption for a simple model and low NA. But striving for a more accurate expression of FDOCM, the Gaussian model, which is based on the paraxial assumption, comes to its limits. Although a Gaussian beam corresponds qualitatively well with the focal volume computed by means of the CTF and a Gaussian field distribution in the generalized aperture, it obscures the clear view on these two fundamental mechanisms. Reasoning in terms of spatial frequencies rather than spatial coordinates turns out to be more illustrative. The convenience of the present model is that the inputs are the illumination and detection modes in the input principal plane of the sample objective, where paraxial assumption can safely be made.

In order to find a simpler expression, we approximated the different wavenumber's CTFs by simply shifting the one of the central wavenumber k_c along s. The true variation of the CTF with k introduces additional imperfections in the tomogram. With the simulation we could, however, verify that the simplified formulation already gave a good indication of the system's performance. It models both effects that limit the signal in the axial direction accurately, which was the purpose of this work.

The axial envelope imposed by the CTF's s-support seems easily to be corrected for numerically by a simple division. Indeed, the lateral blurring is more disturbing since it confuses the sample structure, while the axial envelope is a mere amplitude scaling. Several works [6,7] aim at a digital correction of this lateral blurring with a deconvolution approach. In the work of Ralston *et al.* [8,14], a careful analysis of the FDOCT signal using paraxial Gaussian optics was performed. The defocusing is identified as the source of the lateral blurring of the FDOCT signal. The additional amplitude envelope due to the CTF's s-support seems, however, less evidenced in that approach. The proposed algorithm interpolates the

measured data at each lateral spatial frequency in s in order to correct for the curved CTF support. The FDOCT reconstruction algorithm pretends the spectral data of a given k_p to originate from a single axial spatial frequency. With this interpolation, the spatial frequencies are moved back to their true origin and avoid the defocusing effect.

However, in order to apply digital correction algorithms, the signal first needs to be recorded with a sufficient signal to noise ratio. Both defocusing and the axial envelope decrease the signal amplitude away from the focal plane. Although FDOCT systems have very high sensitivities above 100 dB, the dynamic range is in general limited to about 40 dB [27]. The simulated tomograms presented in this work were all normalized, but in a realistic sample, scatterers with a wide range in scattering strength will be present. In the case of the presented Gaussian system [Fig. 4(a)] with NA=0.5, the signal will be lost about 20 μm off the focal plane even in the most ideal case of a scattering signal that would use the full dynamic range available. Although the refocusing should theoretically increase the 40 dB range to more than 150 μm, it is not possible to record the signal at such out-of-focus positions. A second limitation to this digital post-processing is imposed by the necessary sampling condition. In order to have access to the lateral spatial frequencies over the whole CTF support, the Nyquist criterion has to be fulfilled. Albeit, more critical is the requirement for the phase of the signal, which should be stable over the whole two-dimensional scan. This is a condition that is challenging to meet with a living specimen.

Instead of numerical correction, many hardware attempts to circumvent the limited DOF of FDOCM systems were made. This is equivalent to designing a specific CTF that is better suited for FDOCM rather than correct the artifacts introduced by a less suited CTF. Indeed, with the current model at hand, we are now in the situation to formulate the criteria for the ideal CTF for FDOCM:

- Short s-support
- No curvature
- Smooth lateral envelope

As seen in the simulation results, such a CTF would result indeed in an artifact-free tomogram and should provide an unaltered spatial resolution along an extended DOF. The challenge resides in finding a real CTF approaching this ideal case.

It is interesting to consider which CTFs can be obtained in practice. Assuming circular symmetry, the CTF is a two-dimensional function of q and s, defined however by the two one-dimensional aperture functions of the illumination and detection modes. At each axial frequency s, the CTF is defined by the shifted overlap of the two generalized apertures, sampled as a function of s. The kernel in Eq. (15) further weighs this overlap and projects it along q. The properties of this kernel limit the set of achievable CTFs. If identical illumination and detection apertures are used, the overlap has an additional symmetry, reducing further this available set. Decoupled apertures on the other hand give an additional degree of freedom in designing the system's CTF.

Using Bessel-like beams produced with an axicon lens [28] is a common hardware approach to obtain an extended DOF [9–12]. Such Bessel-like beams indeed propagate over long distances without apparent diffraction and with an invariant radial envelope. Unfortunately, this envelope features many strong sidelobes. Whereas all these works use the identical illumination and detection optics, we have previously reported on an extended focus scheme for FDOCM [13,29], where we use an axicon lens to illuminate the sample, but detection occurs over a decoupled Gaussian aperture. To illustrate the effect of these different optical schemes, the CTFs at the central wavenumber for three configurations are compared in Fig. 8: first a Bessel–Bessel configuration, where both illumination and detection occur through the same optical path comprising an axicon lens; second, the Bessel-like illumination with decoupled Gaussian detection; and, third, a Gaussian confocal configuration, analogous to the previously discussed realistic scenario. For these computations an objective with an NA=0.3 was taken. Using simple plane wave spectrum beam formulation and modeling the axicon as a phase element with a linear phase in the radial direction, we propagated the Bessel-like pattern behind the axicon through a lens to the principal plane of the sample objective, where a ring-like illumination pattern was obtained. Using the formalism of the generalized aperture, the intensity pattern in the focal volume exhibited its first intensity zero in the lateral direction at $\rho=1.3$ μm, and the intensity-FWHM in the axial direction extends over more than 300 μm.

The CTF for the Bessel–Bessel configuration, displayed in Fig. 8(a), approaches the near-ideal scenario [Fig. 5(a)]. The CTF exhibits no curvature and extends over a small range along s only. The drawback of this architecture is revealed when looking at the projection of the CTF along s, revealing the transmission amplitudes of the lateral spatial frequencies in the focal plane. Whereas a large support of lateral spatial frequencies is available, the transmission profile reveals a very strong and narrow

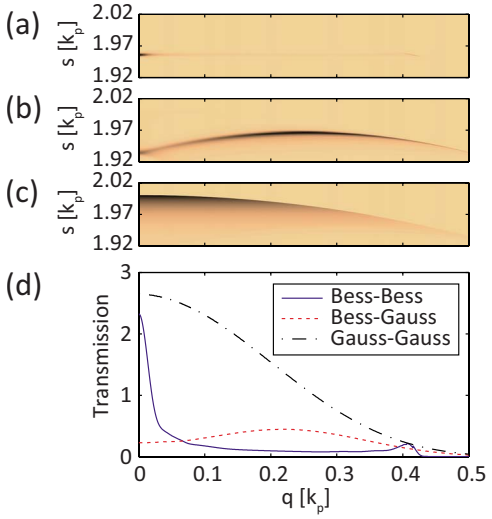

Fig. 8. (Color online) (a)–(c) CTFs at the central wavenumber for (a) Bessel-like illumination and detection, (b) Bessel-like illumination with Gaussian detection, and (c) Gaussian illumination and detection, producing identical in-focus lateral resolutions of 1.3 μm. (d) Projection of the same CTFs along the s direction, evidencing the transmission coefficients for the lateral spatial frequencies for the in-focus plane.

peak at $q=0$ and a second maximum just before the cutoff frequency. Most parts of the large support suffer from a transmission penalty compared to the central peak of up to 30 dB. The limits of the system's dynamic range are thus rapidly reached, and then the large support of spatial frequencies is lost. Even more, the strong central peak corresponds to a very low NA system transmission profile. Disregarding the issue of limited dynamic range, the resulting tomogram is the superposition of a very low NA acquisition and a much fainter high NA signal, rendering a correct interpretation of the tomograms difficult.

The CTF of the decoupled Bessel–Gaussian configuration shown in Fig. 8(b) exhibits curvature, ultimately limiting the DOF by lateral blurring. Compared to the confocal design with identical Gaussian apertures and comparable lateral resolution [Fig. 8(c)], however, the s-support is reduced, significantly increasing the axial signal envelope. Most importantly, the projection of the CTF along s now shows a relatively smooth envelope, resulting in tomograms with good contrast and that are easy to interpret. However, the Gaussian optics still introduces defocusing and limits the scalability to higher NAs.

This study was performed considering a spectral or Fourier domain system, with a discrete wavenumber sampling. This allowed one to express the individual channels as monochromatic waves and simplified the formalism. To extend the reasoning also to time-domain OCT, the time dependence of the expressions has to be maintained in a general way and averaged in order to find the detected intensity signal. This results in an integration along the wavenumber k, analogous to the discrete Fourier transform of the tomogram reconstruction in FDOCT. Together with the variation of the path difference in the reference arm, the outcome is in this case identical to the presented analysis, except that the wavenumber is no longer binned into discrete wavenumber-channels, but represented as a continuous variable.

5. CONCLUSION

In this work, an expression for the FDOCM signal using the principle of the generalized aperture and the CTF was derived. This approach illustrates the spatial frequency sampling of spectral domain OCT. In FDOCM, the signal is acquired in parallel in a set of wavenumber-channels, each defined by its specific CTF. With synthetic tomograms of idealized point-like scatterers it could be shown that the CTF induces a limited DOF by two distinct mechanisms: first, by a defocusing due to its curved shape and, second, by an amplitude envelope, imposed by the width of the CTF along s. Although intrinsically linked, the use of decoupled illumination and detection apertures should allow designing improved CTFs that reduce these disturbing effects and would be better suited for FDOCM than current approaches. The developed model could also serve as a basis for digital post-processing, correcting for the imperfections introduced by non-ideal CTFs. Future developments will show which strategy—CTF design, post-processing, or a combination of both—is more appropriate to overcome the limited DOF in FDOCM.

ACKNOWLEDGMENTS

This research was supported in part by the Swiss National Science Foundation (FNS) 205320- 121922/1 and the European Community's Seventh Framework Programme (FP7/2007-2013) under grant agreement no. 222980.

REFERENCES

1. R. Leitgeb, C. K. Hitzenberger, and A. F. Fercher, "Performance of Fourier domain vs. time domain optical coherence tomography," Opt. Express **11**, 889–894 (2003).
2. J. A. Izatt, M. R. Hee, G. M. Owen, E. A. Swanson, and J. G. Fujimoto, "Optical coherence microscopy in scattering media," Opt. Lett. **19**, 590–592 (1994).
3. S. W. Huang, A. D. Aguirre, R. A. Huber, D. C. Adler, and J. G. Fujimoto, "Swept source optical coherence microscopy using a Fourier domain mode-locked laser," Opt. Express **15**, 6210–6217 (2007).
4. M. A. Choma, A. K. Ellerbee, C. H. Yang, T. L. Creazzo, and J. A. Izatt, "Spectral-domain phase microscopy," Opt. Lett. **30**, 1162–1164 (2005).
5. C. Joo, T. Akkin, B. Cense, B. H. Park, and J. E. de Boer, "Spectral-domain optical coherence phase microscopy for quantitative phase-contrast imaging," Opt. Lett. **30**, 2131–2133 (2005).
6. Y. Yasuno, J. I. Sugisaka, Y. Sando, Y. Nakamura, S. Makita, M. Itoh, and T. Yatagai, "Non-iterative numerical method for laterally superresolving Fourier domain optical coherence tomography," Opt. Express **14**, 1006–1020 (2006).
7. L. F. Yu, B. Rao, J. Zhang, J. P. Su, Q. Wang, S. G. Guo, and Z. P. Chen, "Improved lateral resolution in optical coherence tomography by digital focusing using two-dimensional numerical diffraction method," Opt. Express **15**, 7634–7641 (2007).
8. T. S. Ralston, D. L. Marks, P. S. Carney, and S. A. Boppart, "Interferometric synthetic aperture microscopy," Nat. Phys. **3**, 129–134 (2007).
9. Z. H. Ding, H. W. Ren, Y. H. Zhao, J. S. Nelson, and Z. P. Chen, "High-resolution optical coherence tomography over a large depth range with an axicon lens," Opt. Lett. **27**, 243–245 (2002).
10. K. S. Lee and L. P. Rolland, "Bessel beam spectral-domain high-resolution optical coherence tomography with micro-optic axicon providing extended focusing range," Opt. Lett. **33**, 1696–1698 (2008).
11. L. B. Liu, F. Diaz, L. Wang, B. Loiseaux, J. P. Huignard, C. J. R. Sheppard, and N. G. Chen, "Superresolution along extended depth of focus with binary-phase filters for the Gaussian beam," J. Opt. Soc. Am. A **25**, 2095–2101 (2008).
12. K. M. Tan, M. Mazilu, T. H. Chow, W. M. Lee, K. Taguchi, B. K. Ng, W. Sibbett, C. S. Herrington, C. T. A. Brown, and K. Dholakia, "In-fiber common-path optical coherence tomography using a conical-tip fiber," Opt. Express **17**, 2375–2384 (2009).
13. R. A. Leitgeb, M. Villiger, A. H. Bachmann, L. Steinmann, and T. Lasser, "Extended focus depth for Fourier domain optical coherence microscopy," Opt. Lett. **31**, 2450–2452 (2006).
14. T. S. Ralston, D. L. Marks, P. S. Carney, and S. A. Boppart, "Inverse scattering for optical coherence tomography," J. Opt. Soc. Am. A **23**, 1027–1037 (2006).
15. T. S. Ralston, D. L. Marks, S. A. Boppart, and P. S. Carney, "Inverse scattering for high-resolution interferometric microscopy," Opt. Lett. **31**, 3585–3587 (2006).
16. P. H. Tomlins and R. K. Wang, "Theory, developments and applications of optical coherence tomography," J. Phys. D: Appl. Phys. **38**, 2519–2535 (2005).
17. A. F. Fercher, W. Drexler, C. K. Hitzenberger, and T. Lasser, "Optical coherence tomography—principles and applications," Rep. Prog. Phys. **66**, 239–303 (2003).
18. C. J. R. Sheppard, M. Roy, and M. D. Sharma, "Image for-

mation in low-coherence and confocal interference microscopes," Appl. Opt. **43**, 1493–1502 (2004).
19. J. M. Coupland and J. Lobera, "Holography, tomography and 3d microscopy as linear filtering operations," Meas. Sci. Technol. **19**, 074012 (2008).
20. C. W. McCutchen, "Generalized aperture and the three-dimensional diffraction image," J. Opt. Soc. Am. **54**, 240–244 (1964).
21. C. J. R. Sheppard, M. Gu, Y. Kawata, and S. Kawata, "Three-dimensional transfer functions for high-aperture systems," J. Opt. Soc. Am. A **11**, 593–598 (1994).
22. M. Gu, *Advanced Optical Imaging Theory*, Vol. 75 of Springer Series in Optical Sciences (Springer, 2000).
23. R. A. Leitgeb, R. Michaely, T. Lasser, and S. C. Sekhar, "Complex ambiguity-free Fourier domain optical coherence tomography through transverse scanning," Opt. Lett. **32**, 3453–3455 (2007).
24. A. H. Bachmann, R. A. Leitgeb, and T. Lasser, "Heterodyne Fourier domain optical coherence tomography for full range probing with high axial resolution," Opt. Express **14**, 1487–1496 (2006).
25. B. Baumann, M. Pircher, E. Gotzinger, and C. K. Hitzenberger, "Full range complex spectral domain optical coherence tomography without additional phase shifters," Opt. Express **15**, 13375–13387 (2007).
26. S. Yun, G. Tearney, J. de Boer, and B. Bouma, "Removing the depth-degeneracy in optical frequency domain imaging with frequency shifting," Opt. Express **12**, 4822–4828 (2004).
27. B. Liu and M. E. Brezinski, "Theoretical and practical considerations on detection performance of time domain, Fourier domain, and swept source optical coherence tomography," J. Biomed. Opt. **12**, 044007 (2007).
28. J. H. McLeod, "The axicon—a new type of optical element," J. Opt. Soc. Am. **44**, 592–597 (1954).
29. M. Villiger, J. Goulley, M. Friedrich, A. Grapin-Botton, P. Meda, T. Lasser, and R. A. Leitgeb, "*In vivo* imaging of murine endocrine islets of langerhans with extended-focus optical coherence microscopy," Diabetologia **52**, 1599–1607 (2009).